Water oxidation at hematite photoelectrodes with an iridium based catalyst

Laura Badia-Bou,[1] Elena Mas-Marza,[2] Pau Rodenas,[1] Eva M. Barea,[1] Francisco-Fabregat-Santiago,[1] Sixto Gimenez[1]*, Eduardo Peris[2]*, Juan Bisquert[1]*

[1]Photovoltaics and Optoelectronic Devices Group, Departament de Física, Universitat Jaume I, 12071 Castelló, Spain

[2]Departament de Química Inorgànica & Orgànica, Universitat Jaume I, 12071, Castelló, Spain

Email: sjulia@uji.es, eperis@uji.es, bisquert@uji.es

29 January 2013

Abstract

The iridium complex $[Cp^*Ir(H_2O)_3](SO_4)$ was used as an organometallic source for the electrodeposition of iridium oxide onto Fe_2O_3. The new iridium-containing electrode allowed us to study the coupling between the photocatalytic properties of hematite with the electrocatalytic properties of the iridium-based material. A cathodic shift of the photocurrent for water oxidation upon electrodeposition of the iridium complex was observed, which increased with increasing surface concentration of IrO_x on Fe_2O_3. The shift for the highest surface concentration of iridium tested amounts to 300 mV at 200 $\mu A \cdot cm^{-2}$ current density. The catalytic mechanism of the IrO_x layer was unveiled by impedance spectroscopy measurements fitted to a physical model, and can be explained on the basis of a highly capacitive layer, which enhances charge separation and stores photogenerated holes at Fe_2O_3, subsequently oxidizing water. These findings improve our understanding of the mechanism of water oxidation by heterogenous Ir-based catalysts coupled to semiconductor electrodes.

Introduction

The efficient generation of hydrogen by photoelectrochemical water splitting with semiconductor materials has become one of the strategic scientific and technological key-targets in order to face the energy problem in the forthcoming years.[1-4] Inspired by photosynthesis, this approach relies on the harvesting of solar energy and its storage in the form of chemical bonds to produce solar fuels, which can be used upon demand. In order to achieve this goal, a semiconductor material must satisfy certain stringent requirements including: i) visible light absorption, ii) appropriate positions of the conduction and valence band energy levels with respect to the relevant reaction potentials, iii) efficient charge separation, iv) good transport properties, v) facile interfacial charge-transfer kinetics, and vi) good stability in contact with aqueous solutions.[4] To date, no single material has fulfilled all the required conditions.

Hematite has shown extraordinary promising properties for solar water splitting due to its combination of abundance, visible light absorption (up to ~600 nm), stability in harsh conditions, and a valence band energy level sufficiently low to oxidize water.[5-7] These advantageous properties are balanced by its inherent low conductivity, and a low energy level conduction band incapable of reducing H_2. The low conductivity of hematite together with its high light penetration depth can be overcome by nanostructuring strategies, which orthogonalize light absorption and carrier collection. As an example, one dimensional core-shell structures like Fe_2O_3 coated Ti_2Si nanonets have shown improved performances.[8] On the other hand, raising the energy of electrons to facilitate the reduction of H_2 can be achieved by applying an external bias with a photovoltaic device, or by integrating a small bandgap water-reduction system in a tandem configuration.[9]

Photoelectrochemical water oxidation at hematite electrodes also requires a large applied potential to produce a photocurrent. This large "overpotential" is believed to be caused by sluggish water oxidation kinetics at the hematite surface which competes with surface state recombination.[10,11] Consequently, different surface treatments (deposition of 13-group oxide overlayers,[12] deposition of tiny layers of p-hematite[13]) and addition of catalysts (cobalt ions, the cobalt phosphate catalyst, "Co-Pi"[14-16] and IrO_2[17]) have been applied in order to minimize this problem.

Ir-based catalysts appear as ideal systems, located at the top end of the volcano plot for water oxidation catalysts by Trasatti.[4,18] Particularly, iridium oxides have the highest activities and turnover frequencies.[19] For the electrodeposition of iridium oxide films several methods have been reported,[20-31] but recently Crabtree and Brudvig demonstrated that

$[Cp^*Ir(H_2O)_3](SO_4)$ (Scheme 1) is an excellent precursor for an amorphous electrodeposited iridium catalyst.[32] In fact, they have highlighted the benefits of using iridium-based organometallic species as convenient sources of electrodeposited iridium oxides. They also have demonstrated that the cyclic voltammetric response of the electrodeposited material depends on the nature of the organometallic precursor used and do not match, in either case, with the responses given by iridium oxide anodes prepared from non-organometallic precursors.[32]

Different pentamethylcyclopentadienyl (Cp*) derivatives have demonstrated to be robust and highly active homogeneous catalysts for water oxidation when driven with cerium(IV)[33-36] and sodium periodate[37,38] as primary oxidants. Additionally, insight into the catalytic mechanisms (homogeneous *vs* heterogeneous catalysis) has become accessible by monitoring mass gain of the test electrodes by Electron Quartz Nanobalance (EQCN).[39,40]

In the present study, we have electrodeposited iridium oxide onto a Fe_2O_3 electrode using $[Cp^*Ir(H_2O)_3](SO_4)$ as the iridium source. Our initial aim is to study whether there should be any coupling between the photocatalytic properties of hematite with the electrocatalytic properties of the iridium electrodeposited material. Our final goal is the preparation of efficient photoanodes, to be integrated in water splitting photoelectrochemical solar cells. For this purpose, the electrodes must oxidize water with minimum overpotentials, affording large oxygen evolution rates upon solar illumination. Complementarily, we want to evaluate the effect of the iridium catalyst electrodeposited onto hematite in order to improve our understanding about the mechanisms operating in the water oxidation catalysis.

Experimental method

Hematite films were deposited onto FTO substrates (SnO_2:F, TEC 15) by Atmospheric Pressure Chemical Vapor Deposition (APCVD)[17,41] using $5 \cdot 10^{-3}$ mol $Fe(CO)_5$ as iron precursor and TEOS (TetraEthylOrtoSilicate) as Si doping agent (8 mol-%). Prior to hematite deposition, the FTO substrates were exposed to ozone plasma during 30 min. Subsequently, the substrates were immersed into a 40 mM titanium chloride tetrahydrofuyran complex solution during 30 min at 70 ºC. Then, the substrates were heated at 400 ºC in a hot plate and APCVD deposition took place. The reactive and carrier gases were directed vertically onto the heated substrate at 0.1 bar pressure.

The iridium oxide was electrodeposited onto Fe_2O_3 electrodes in a three electrode cell from a solution of $[Cp^*Ir(H_2O)_3](SO_4)$ in 0.1M KNO_3. Different surface concentrations of the catalyst on the surface of Fe_2O_3 were obtained, depending on the concentration of the

organometallic iridium source in the solution (5 μM, 10 μM, 1 mM and 5 mM). For electrodeposition, Fe_2O_3 was the working electrode, graphite was used as counter electrode, and a Ag/AgCl electrode was used as reference. Deposition was carried out by applying 2V vs. Ag/AgCl during 1 hour from the different [IrCp*]-containing solutions. After deposition the samples were rinsed in water and dried with air.

Cyclic voltammetry, steady state current density voltage (j-V) and Electrochemical Impedance Spectroscopy (EIS) were carried out using a FRA equipped PGSTAT-30 from Metrohm Autolab. A three-electrode configuration was used, where the Fe_2O_3/Ir photo-electrode was connected to the working electrode, a Pt wire was connected to the counterelectrode and a saturated Ag/AgCl was used as the reference electrode. An aqueous solution buffered to pH 7 using a 0.1M phosphate buffer (KH_2PO_4/K_2HPO_4) was used as electrolyte. Cyclic voltammetry measurements were carried out at 10 $mV \cdot s^{-1}$ unless otherwise stated. All the electrochemical measurements were referred to the reversible hydrogen electrode (RHE) by the equation $V_{RHE} = V_{Ag/AgCl} + 0.197 + pH(0.059)$. The electrodes were illuminated using a 450W Xe lamp. The light intensity was adjusted with a thermopile to 100 mW/cm^2, with illumination through the substrate. Consequently, there was no competition between Fe_2O_3 and the Iridium layer to absorb visible light.

Results and discussion

Figure 1a shows a cross section of a representative FTO/Fe_2O_3 film. The thickness of the Fe_2O_3 layer is around 300 nm, and its morphology appears as the cauliflower-like structures previously reported by Gratzel and coworkers.[17,41] XRD has confirmed the monophase nature of the material, α-Fe_2O_3 as illustrated in Figure 1b.

The optical properties of the material are shown in Figure 2. The optical bandgap could be estimated by the Tauc plot for indirect bandgap transitions[42] ($r = 1/2$) (Figure 2b). The obtained value was E_g = 2.1 eV in excellent agreement with the reported values for hematite, E_g = 2.1-2.2 eV.[43]

After the electrodeposition of the iridium complex, a clear darker layer appears on top of the reddish hematite, which was previously identified as blue layer (BL).[32] Surface analyses of selected Fe_2O_3 samples with electrodeposited iridium oxides obtained from 10 μM, 1 mM and 5 mM [Cp*Ir] solutions were carried out by XPS. An example of the obtained spectra is shown in Supporting Information, Figure SI1. The surface concentration of Ir was estimated as 0.48 at-%, 3.9 at-% and 5.7 at-% , respectively. The carbon content in the electrodeposited iridium material may be originated from carboxylic-acid oxidation product functioning as a

O-donor to iridium.[39] Additionally, carbonate species may originate from the oxidative degradation of the Cp* ligand.[32] A significant contribution of the O signal can be ascribed to the Ir-O bonding, and after spectra deconvolution, the obtained stoichiometry for the deposited IrO_x phase is x = 2.1, x = 2.2 and x=2.1 for 10 μM, 1 mM and 5 mM solutions, respectively. Moreover, the analysis of the Fe signal confirmed the stoichiometry of the Fe_2O_3 phase in all cases.

The photoelectrochemical properties of the Fe_2O_3 specimens before and after electrodeposition of different amounts of iridium were tested by cyclic voltammetry. Although the electrodeposited IrO_x layer absorbs visible light (see Supporting Information, Figure SI2), since samples were illuminated through the substrate, there was no competition between Fe_2O_3 and the IrO_x layer to absorb visible light. Figure 3 shows the results obtained in the dark and under illumination. Upon deposition of the iridium material from low concentrated solutions (5 μM and 10 μM), two distinct features can be observed in the dark j-V curves (Figure 3a). First, the catalytic wave for water oxidation at 1.7 V *vs* RHE is enhanced by the addition of iridium. Second, the capacitive feature centered at 0.8 V *vs* RHE is in good agreement with previous studies with iridium oxide films. This reversible wave has been ascribed to a Ir(III)/Ir(IV) redox process, which involves a two-electron, three proton process.[32,44] Under illumination (Figure 3b), a cathodic shift of the onset potential for water oxidation takes place upon Ir addition, which increases with the electrodeposited Ir content. At high [Cp^*Ir] concentrations (1 mM, 5 mM), both in the dark (Figure 3c) and under illumination (Figure 3d), the electrode behavior is dominated by the large capacitance stemming from the Ir(III)/Ir(IV) redox process,[45,46] and water oxidation clearly takes place at more cathodic potentials as the Ir content increases in the film.

A clearer picture of the photoelectrochemical behavior of the tested samples is provided by the steady-state j-V curves. For these measurements, the photocurrent was sampled after stabilizing over several minutes for individual potentials and the obtained results are showed in Figure 4a. Direct comparison of the steady-state j-V curve and cyclic voltammetry curves of Figure 3 is presented as Figure 4b and Figure 4c for Fe_2O_3 samples after electrodeposition of [Cp*Ir] from 10 μM and 1 mM solutions, respectively. For the other concentrations, results are showed as Supporting Information, Figure SI3. In all cases, the obtained agreement is very good. The higher values of photocurrent obtained for some of the steady-state j-V curves at high anodic bias indicate some diffusion limitations, which have been highlighted elsewhere.[47] On the other hand, from these steady-state j-V curves, the beneficial effect of [Cp*Ir] cathodically shifting the potential for water oxidation is even more evident compared

to cyclic voltammetry curves, since the effect of capacitance is absent. As a reference, the potentials needed to sustain a photocurrent of 200 $\mu A \cdot cm^{-2}$ (dotted line in Figure 4) are compiled in Table 1 together with the cathodic shifts with respect to bare hematite (ΔV). These values are in reasonable good correspondence with those derived from Figure 3. Moreover, the cathodic shifts obtained in the present study are in excellent agreement with those reported by Tilley et al. after electrophoretic deposition of IrO_2 nanoparticles.[17] In that study, 200 mV cathodic shift was reported for a surface concentration of 1 at-% Iridium, while 130 mV are obtained in the present study for 0.5 at-% Iridium. At high concentrations of Ir (electrodeposition from 1 mM and 5 mM solutions), a remarkable 300 mV cathodic shift is obtained.

Further evidence to assign the steady-state photocurrent to water oxidation was carried out by running cyclic voltammetry curves with the initial potential at the onset potential for the photocurrent (V_0). This representation allows a clear deconvolution of the IrO_x capacitive processes ($V<V_0$) and the faradaic water oxidation process ($V>V_0$). An example is showed in Figure 4d for Fe_2O_3/IrO_x (from 1 mM solution). The first two scans at $V>V_0$ and $V<V_0$ are represented together with the steady-state j-V curve, clearly indicating that $V>V_0$ correspond to water oxidation. Additionally, in order to rule out other possible processes (i.e. IrO_x oxidation), 20 consecutive cyclic voltammetry scans were carried out under illumination for samples with different surface concentrations of Iridium. The results are showed as Supporting Information, Figure SI4. At low Ir concentration (deposition from 10 μM [Cp*Ir] solution), the repeatability of the scans clearly indicated that the IrO_x layer was stable and did not oxidize during testing. At high Ir concentrations (deposition from 1 mM [Cp*Ir] solution), there was a systematic shift of the cyclic voltammetry curves with the number of cycles. This suggests that progressive oxidation of the Iridium-based layer took place during photoelectrochemical testing. However, this effect is clearly separated from the steady-state photocurrent for water oxidation reported in Figure 4.

Further insight into the water oxidizing mechanisms was provided by electrochemical impedance spectroscopy (EIS). In order to analyse the physico-chemical processes responsible for the traffic of carriers within the material and at the interface with the aqueous solution, a physical model is required. We already developed a physical model, which accounted for the relevant processes leading to water oxidation for Fe_2O_3 synthesized by atomic layer deposition (Supporting Information, Figure SI5).[10,11,16] The equivalent circuit (EC) consists of the capacitance of the bulk hematite, C_{bulk}, charge transfer resistance from the valence band of the hematite, $R_{ct,bulk}$, a resistance which is related to the rate of trapping

holes in surface states, R_{trap}, a capacitance of the surface states, C_{trap}, charge transfer resistance from the surface states, $R_{ct,trap}$.[11] We showed that the photocurrent onset was coincident with the charging of a surface state and the decrease of the charge transfer resistance from this surface state, $R_{ct,trap}$. This behavior clearly indicated that hole transfer predominantly takes place by a surface state. In the present study, identical behavior was observed (Figure 5), and consequently, analogous water oxidation mechanism can be safely proposed for APCVD hematite.

Experimentally, we did not observe the presence of any additional arc in the obtained Nyquist plots after the deposition of the IrO_x layer compared to bare Fe_2O_3. However, in order to account for the presence of this IrO_x layer, we will now consider the model scheduled by the EC shown in Figure 6. This EC is similar to that developed for bare hematite, and includes some extra elements in order to account for the IrO_x layer: the capacitance of the IrO_x layer, C_{IrOx}, and charge transfer resistance from the IrO_x layer, $R_{ct,IrOx}$. In order to unambiguously fit the experimental impedance spectra obtained, we have defined the capacitance of the Fe_2O_3/IrO_x layer, as $C_{film} = C_{bulk} + C_{trap} + C_{IrOx}$, and the charge transfer resistance from the film, R_{ct} as the parallel combination of $R_{ct,trap}$ and $R_{ct,\ IrOx}$. Consequently, the analyzed circuit is similar to that scheduled in Supporting Information, Figure SI5d.

Some examples of the Nyquist plots experimentally obtained together with the fittings to the employed physical models for the tested samples are compiled as Supporting Information, Figure SI6. The quality of the fitting to the experimental spectra was systematically good for all the tested samples, with fitting errors below 5% for all the extracted parameters. The results obtained from fitting the experimental impedance to the model scheduled in Figure 6 are shown in Figure 7.

It is clear that C_{film} is dominated by the capacitance of the IrO_x layer (C_{IrOx}) at low potentials (0.5 -1.2 V vs RHE), since this capacitance is increasing with the thickness of the IrO_x layer (Figure 7a and Figure 7c). The peaks at 0.8 V - 0.9 V vs RHE, are consistent with the reversible wave observed by cyclic voltammetry shown in Figure 3, corresponding to the Ir(III)/Ir(IV) redox process. This capacitance is also responsible for the hysteresis observed in the cyclic voltammetry curves (Figure 3), particularly at high surface concentrations of Ir.

After the deposition of low amounts of the Ir-complex onto hematite (from 5 μM and 10 μM solutions), the same correlation shown in Figure 5 is obtained between the photocurrent onset, C_{film} and R_{ct} (Supporting Information, Figure SI2). The lower R_{ct} values (Figure 7b) satisfactorily explain the cathodic shift of the photocurrent for water oxidation observed in Figure 3 and Figure 4. At higher Ir concentrations (from 1 mM, 5 mM solutions), the

capacitance of the IrO_x layer becomes very large and clearly dominates the capacitance of the electrode. A close look at Figure 7b and Figure 7d indicates that the charge transfer resistance decreases upon increasing the iridium concentration on the Fe_2O_3 surface, reflecting that Fe_2O_3 photogenerated holes may be efficiently transferred to the IrO_x layer, where water oxidation takes place. This supports the idea that the process follows a similar mechanism as that recently proposed for the effect of the Co-Pi catalyst.[16] The low values of R_{ct} are responsible for the photocurrents of 0.2 $mA \cdot cm^{-2}$ for water oxidation at potentials as low as 1.3 V vs RHE (Figure 4).

Moreover, it is relevant to determine whether the cathodic shift produced upon Ir electrodeposition is related to a shift of the conduction band due to the presence of a dielectric layer. Consequently, we analyzed the behavior of the bulk capacitance of Fe_2O_3 (C_{bulk}) in the dark, as shown in the Mott-Schottky plot of Figure 8. For the different concentrations of Ir employed, the donor density (N_D) and flat band potential (V_{FB}) were compared (Table 2). From the comparison of the data, it can be inferred that the V_{FB} value does not depend on the concentration of iridium, therefore indicating that the cathodic shift is not due to a conduction band shift. A similar behavior was observed upon deposition of the Co-Pi catalyst on Fe_2O_3.[16] Additionally, these values of flat band potential are in good agreement with previously reported values for hematite synthetized by different processes.[10,11,16] The high values of N_D ($\sim 10^{22}$ cm^{-3}) for these films are in reasonable good agreement with the values reported for APCVD hematite (10^{20}-10^{21} cm^{-3}).[48,49]

All these experiments support the idea that the catalytic effect of the IrO_x layer can be interpreted in terms of a highly capacitive layer. This layer stores the photogenerated holes at Fe_2O_3 by oxidation of Ir(III) to Ir(IV). Consequently, the transfer of photogenerated holes to the IrO_x layer significantly reduces recombination with conduction band electrons, which is responsible for the beneficial cathodic shift observed for water oxidation.

Conclusions

In this work, we synthesized APCVD Fe_2O_3 films and we evaluated the effect of an electrodeposited [Cp*Ir] catalyst on the photoelectrochemical water oxidation performance. Structural and surface analysis of the electrodeposited films showed that the Ir layer preferentially possesses stoichiometry IrO_x, with $x \approx 2.1$ for the Ir-containing layers obtained from solutions with different concentrations of the [$IrCp^*$] source. The cathodic potential shift for the water photo-oxidation increased upon increasing the amount of the electrodeposited Ir catalyst. Remarkably, 300 mV shift at 200 $\mu A \cdot cm^{-2}$ photocurrent was obtained for the highest

surface concentrations of IrO_x tested. We have interpreted the catalytic mechanism of the iridium containing film on the basis of a highly capacitive layer, which enhances charge separation and can store photogenerated holes at Fe_2O_3, subsequently oxidizing water, with lower surface recombination compared to bare Fe_2O_3. These findings constitute an important step forward in the understanding of the mechanism operating in the water oxidation by heterogenous Ir-based catalysts coupled with semiconductor materials.

Acknowledgements

JB acknowledges support by projects from Ministerio de Economía y Competititvidad (MINECO) of Spain (Consolider HOPE CSD2007-00007), and Generalitat Valenciana (PROMETEO/2009/058). FFS. thanks the funding of University Jaume I- Bancaixa (Grant P1·1B2011-50).SG acknowledges support by MINECO of Spain under the Ramon y Cajal programme. Mrs. Encarna Blasco from the Instituto Tecnológico de Cerámica is acknowledged for carrying out the structural characterization by XPS. The SCIE of Universidad de Valencia is acknowledged for the SEM images.

References

(1) Barber, J. *Chemical Society Reviews* **2009**, *38*, 185.

(2) Chen, X. B.; Shen, S. H.; Guo, L. J.; Mao, S. S. *Chemical Reviews* **2010**, *110*, 6503.

(3) van de Krol, R.; Liang, Y. Q.; Schoonman, J. *Journal of Materials Chemistry* **2008**, *18*, 2311.

(4) Walter, M. G.; Warren, E. L.; McKone, J. R.; Boettcher, S. W.; Mi, Q. X.; Santori, E. A.; Lewis, N. S. *Chemical Reviews* **2010**, *110*, 6446.

(5) Hamann, T. W. *Dalton Transactions* **2012**, *41*, 7830.

(6) Sivula, K.; Le Formal, F.; Gratzel, M. *Chemsuschem* **2011**, *4*, 432.

(7) Lin, Y. J.; Yuan, G. B.; Sheehan, S.; Zhou, S.; Wang, D. W. *Energy & Environmental Science* **2011**, *4*, 4862.

(8) Lin, Y. J.; Zhou, S.; Sheehan, S. W.; Wang, D. W. *Journal of the American Chemical Society* **2011**, *133*, 2398.

(9) Alexander, B. D.; Kulesza, P. J.; Rutkowska, L.; Solarska, R.; Augustynski, J. *Journal of Materials Chemistry* **2008**, *18*, 2298.

(10) Klahr, B.; Gimenez, S.; Fabregat-Santiago, F.; Bisquert, J.; Hamann, T. W. *Energy & Environmental Science* **2012**, *5*, 7626.

(11) Klahr, B.; Gimenez, S.; Fabregat-Santiago, F.; Hamann, T.; Bisquert, J. *Journal of the American Chemical Society* **2012**, *134*, 4294.

(12) Hisatomi, T.; Le Formal, F.; Cornuz, M.; Brillet, J.; Tetreault, N.; Sivula, K.; Graetzel, M. *Energy & Environmental Science* **2012**, *4*, 2512.

(13) Lin, Y. J.; Xu, Y.; Mayer, M. T.; Simpson, Z. I.; McMahon, G.; Zhou, S.; Wang, D. W. *Journal of the American Chemical Society* **2012**, *134*, 5508.

(14) Kanan, M. W.; Nocera, D. G. *Science* **2008**, *321*, 1072.

(15) Zhong, D. K.; Cornuz, M.; Sivula, K.; Graetzel, M.; Gamelin, D. R. *Energy & Environmental Science* **2012**, *4*, 1759.

(16) Klahr, B.; Gimenez, S.; Fabregat-Santiago, F.; Bisquert, J.; Hamann, T. W. *Journal of the American Chemical Society* **2012**, *134*, 16693.

(17) Tilley, S. D.; Cornuz, M.; Sivula, K.; Gratzel, M. *Angewandte Chemie-International Edition* **2010**, *49*, 6405.

(18) Trasatti, S. *Journal of Electroanalytical Chemistry* **1980**, *111*, 125.

(19) Mills, A.; Russell, T. *Journal of the Chemical Society-Faraday Transactions* **1991**, *87*, 1245.

(20) Zhao, Y. X.; Hernandez-Pagan, E. A.; Vargas-Barbosa, N. M.; Dysart, J. L.; Mallouk, T. E. *Journal of Physical Chemistry Letters* **2011**, *2*, 402.

(21) Zhao, Y. X.; Vargas-Barbosa, N. M.; Hernandez-Pagan, E. A.; Mallouk, T. E. *Small* **2011**, *7*, 2087.

(22) Nakagawa, T.; Beasley, C. A.; Murray, R. W. *Journal of Physical Chemistry C* **2009**, *113*, 12958.

(23) Profeti, D.; Lassali, T. A. F.; Olivi, P. *Journal of Applied Electrochemistry* **2006**, *36*, 883.

(24) Sardar, K.; Fisher, J.; Thompsett, D.; Lees, M. R.; Clarkson, G. J.; Sloan, J.; Kashtiban, R. J.; Walton, R. I. *Chemical Science* **2011**, *2*, 1573.

(25) Mugavero, S. J.; Smith, M. D.; Yoon, W. S.; zur Loye, H. C. *Angewandte Chemie-International Edition* **2009**, *48*, 215.

(26) Trasatti, S. *Electrochimica Acta* **1984**, *29*, 1503.

(27) Stonehar.P; Kozlowsk.Ha; Conway, B. E. *Proceedings of the Royal Society of London Series a-Mathematical and Physical Sciences* **1969**, *310*, 541.

(28) Rand, D. A. J.; Woods, R. *Journal of Electroanalytical Chemistry* **1974**, *55*, 375.

(29) Capon, A.; Parsons, R. *Journal of Electroanalytical Chemistry* **1972**, *39*, 275.

(30) Buckley, D. N.; Burke, L. D. *Journal of the Chemical Society-Faraday Transactions I* **1975**, *71*, 1447.

(31) Pickup, P. G.; Birss, V. I. *Journal of Electroanalytical Chemistry* **1987**, *220*, 83.

(32) Blakemore, J. D.; Schley, N. D.; Olack, G. W.; Incarvito, C. D.; Brudvig, G. W.; Crabtree, R. H. *Chemical Science* **2011**, *2*, 94.

(33) Hull, J. F.; Balcells, D.; Blakemore, J. D.; Incarvito, C. D.; Eisenstein, O.; Brudvig, G. W.; Crabtree, R. H. *Journal of the American Chemical Society* **2009**, *131*, 8730.

(34) Hetterscheid, D. G. H.; Reek, J. N. H. *Chemical Communications*, *47*, 2712.

(35) McDaniel, N. D.; Coughlin, F. J.; Tinker, L. L.; Bernhard, S. *Journal of the American Chemical Society* **2008**, *130*, 210.

(36) Blakemore, J. D.; Schley, N. D.; Balcells, D.; Hull, J. F.; Olack, G. W.; Incarvito, C. D.; Eisenstein, O.; Brudvig, G. W.; Crabtree, R. H. *Journal of the American Chemical Society* **2010**, *132*, 16017.

(37) Parent, A. R.; Brewster, T. P.; De Wolf, W.; Crabtree, R. H.; Brudvig, G. W. *Inorganic Chemistry*, *51*, 6147.

(38) Hintermair, U.; Hashmi, S. M.; Elimelech, M.; Crabtree, R. H. *Journal of the American Chemical Society*, *134*, 9785.

(39) Blakemore, J. D.; Schley, N. D.; Kushner-Lenhoff, M. N.; Winter, A. M.; D'Souza, F.; Crabtree, R. H.; Brudvig, G. W. *Inorganic Chemistry* **2012**, *51*, 7749.

(40) Schley, N. D.; Blakemore, J. D.; Subbaiyan, N. K.; Incarvito, C. D.; D'Souza, F.; Crabtree, R. H.; Brudvig, G. W. *Journal of the American Chemical Society* **2011**, *133*, 10473.

(41) Kay, A.; Cesar, I.; Graetzel, M. *Journal of the American Chemical Society*

2006, *128*, 15714.

(42) Chen, Z. B.; Jaramillo, T. F.; Deutsch, T. G.; Kleiman-Shwarsctein, A.; Forman, A. J.; Gaillard, N.; Garland, R.; Takanabe, K.; Heske, C.; Sunkara, M.; McFarland, E. W.; Domen, K.; Miller, E. L.; Turner, J. A.; Dinh, H. N. *Journal of Materials Research* **2010**, *25*, 3.

(43) Hardee, K. L.; Bard, A. J. *Journal of the Electrochemical Society* **1976**, *123*, 1024.

(44) Burke, L. D.; Whelan, D. P. *Journal of Electroanalytical Chemistry* **1981**, *124*, 333.

(45) Hu, C. C.; Huang, Y. H.; Chang, K. H. *Journal of Power Sources* **2002**, *108*, 117.

(46) Lokhande, C. D.; Dubal, D. P.; Joo, O.-S. *Current Applied Physics* **2011**, *11*, 255.

(47) Shimizu, K.; Lasia, A.; Boily, J. F. *Langmuir*, *28*, 7914.

(48) Cesar, I.; Sivula, K.; Kay, A.; Zboril, R.; Graetzel, M. *Journal of Physical Chemistry C* **2009**, *113*, 772.

(49) Le Formal, F.; Tetreault, N.; Cornuz, M.; Moehl, T.; Gratzel, M.; Sivula, K. *Chemical Science* **2011**, *2*, 737.

Table captions

Table 1.- Potential required to sustain a photocurrent of 200 μA·cm^{-2} from the steady-state j-V curves in Figure 4 for bare hematite (Ref) and after electrodeposition of [Cp*Ir] from solutions with different concentrations (5 μM, 10 μM, 1 mM and 5 mM). The cathodic shift (ΔV) with respect to bare hematite is also indicated.

Table 2.- Flat band potential (V_{FB}) and donor density (N_D) for Fe_2O_3 before (Ref) and after electrodeposition of [Cp*Ir] from solutions with different concentrations (5 μM, 10 μM, 1 mM and 5 mM).

Figure captions

Figure 1.- (a) SEM micrograph of a cross section of FTO/Fe_2O_3. (b) XRD spectrum of a FTO/Fe_2O_3 sample. All the diffraction peaks were identified corresponding to FTO (□) and Fe_2O_3 (•) phases.

Figure 2.- (a) Optical density of a FTO/Fe_2O_3 representative sample, (b) Tauc plot for an indirect bandgap semiconductor, $r = 1/2$ indicating a value E_g = 2.1 eV for hematite.

Figure 3.- Cyclic voltammetry curves obtained in the dark and under illumination at 100 mW·cm^{-2} for a reference Fe_2O_3 sample (Ref) and after electrodeposition of [Cp*Ir] from solutions with different concentrations. The scan rate was 10 mV·s^{-1}. (a) 5 μM and 10 μM in the dark (b) 5 μM and 10 μM under illumination, (c) 1 mM and 5 mM in the dark, (d) 1 mM and 5 mM under illumination.

Figure 4.- (a) Steady-state j-V curves for bare Fe_2O_3 (Ref) and after electrodeposition of [Cp*Ir] from solutions with different concentrations (5 μM, 10 μM, 1 mM and 5 mM). The lines are included as eyeguides. Comparison between cyclic voltammetry (lines) and steady-state (red dots) j-V curves for Fe_2O_3 samples after electrodeposition of [Cp*Ir] from solutions with different [Cp*Ir] concentrations (b) 10 μM and (c) 1 mM. (d) Cyclic voltammetry curves with the starting potential at the photocurrent onset (V_0) and steady state j-V curves for Fe_2O_3/IrOx sample after electrodeposition of [Cp*Ir] from 1 mM solution.

Figure 5.- Photocurrent (j), charge transfer resistance from a surface state ($R_{ct,trap}$) and trap capacitance (C_{trap}) for a reference hematite sample.

Figure 6.- Equivalent circuit employed for the interpretation of hematite electrodes coated with a IrO_x catalyst.

Figure 7.- Capacitance, C_{film} (a and c) and charge transfer resistance, R_{ct} (b and d) for the Fe_2O_3/IrO_x films from low concentrated solutions (a and b) and high concentrated solutions (c and d).

Figure 8.- Mott-Schottky plot of the bulk capacitance of hematite, after deposition of a IrO_x layer from solutions with different concentrations of the [Cp*Ir] catalyst (5 μM, 10 μM and 1 mM). The results for bare hematite are also included as a reference.

Table 1.

Sample	V@j= 200 μA·cm^{-2} (V vs RHE)	ΔV (mV)
Ref	1.58	0
5 μM	1.46	129
10 μM	1.45	130
1 mM	1.29	300
5 mM	1.29	300

Table 2.-

Sample	V_{FB} (V vs RHE)	N_D (·10^{22} cm^{-3})
Ref	0.71	1.87
5 μM	0.67	1.98
10 μM	0.70	1.87
1 mM	0.70	1.92

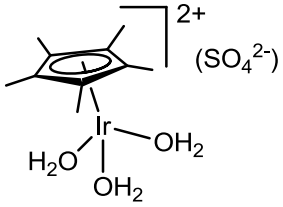

Scheme 1

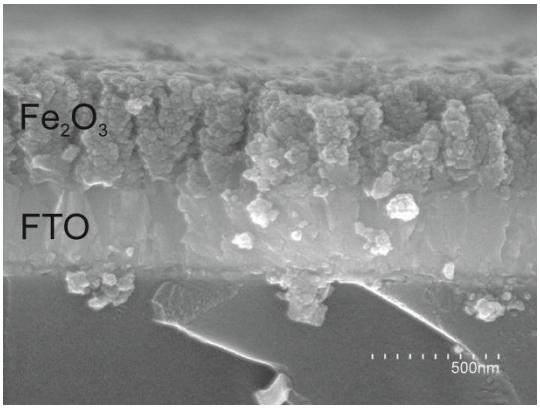
Fe2O3
FTO
500nm

(a)

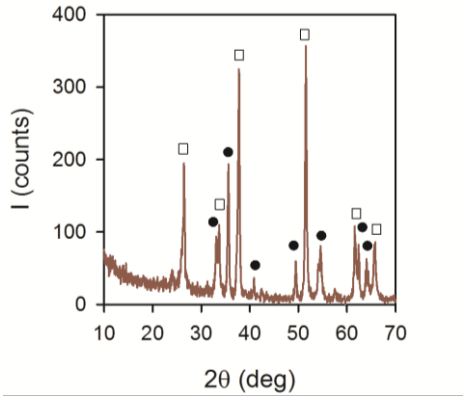
400
300
200
100
0
I (counts)
10
20
30
40
50
60
70
2θ (deg)

(b)

Fig. 1

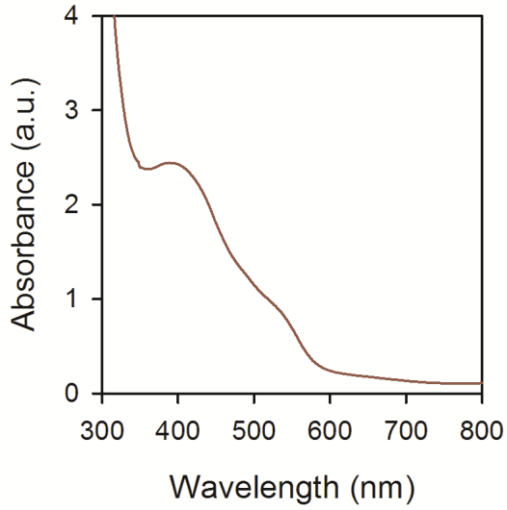
Absorbance (a.u.)
Wavelength (nm)
0
1
2
3
4
300
400
500
600
700
800

(a)

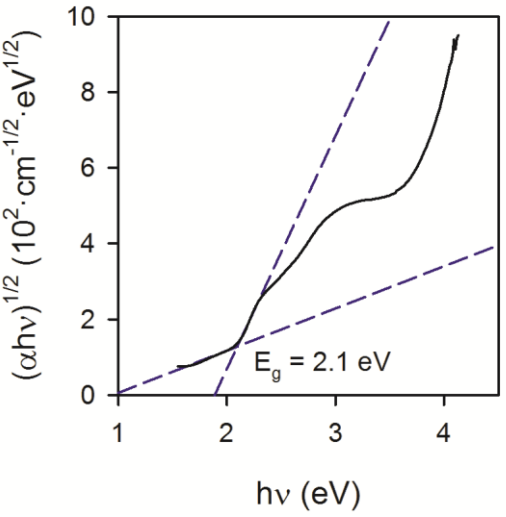
$(\alpha h\nu)^{1/2}$ ($10^2 \cdot cm^{-1/2} \cdot eV^{1/2}$)
$h\nu$ (eV)
E_g = 2.1 eV
0
2
4
6
8
10
1
2
3
4

(b)

Fig. 2.

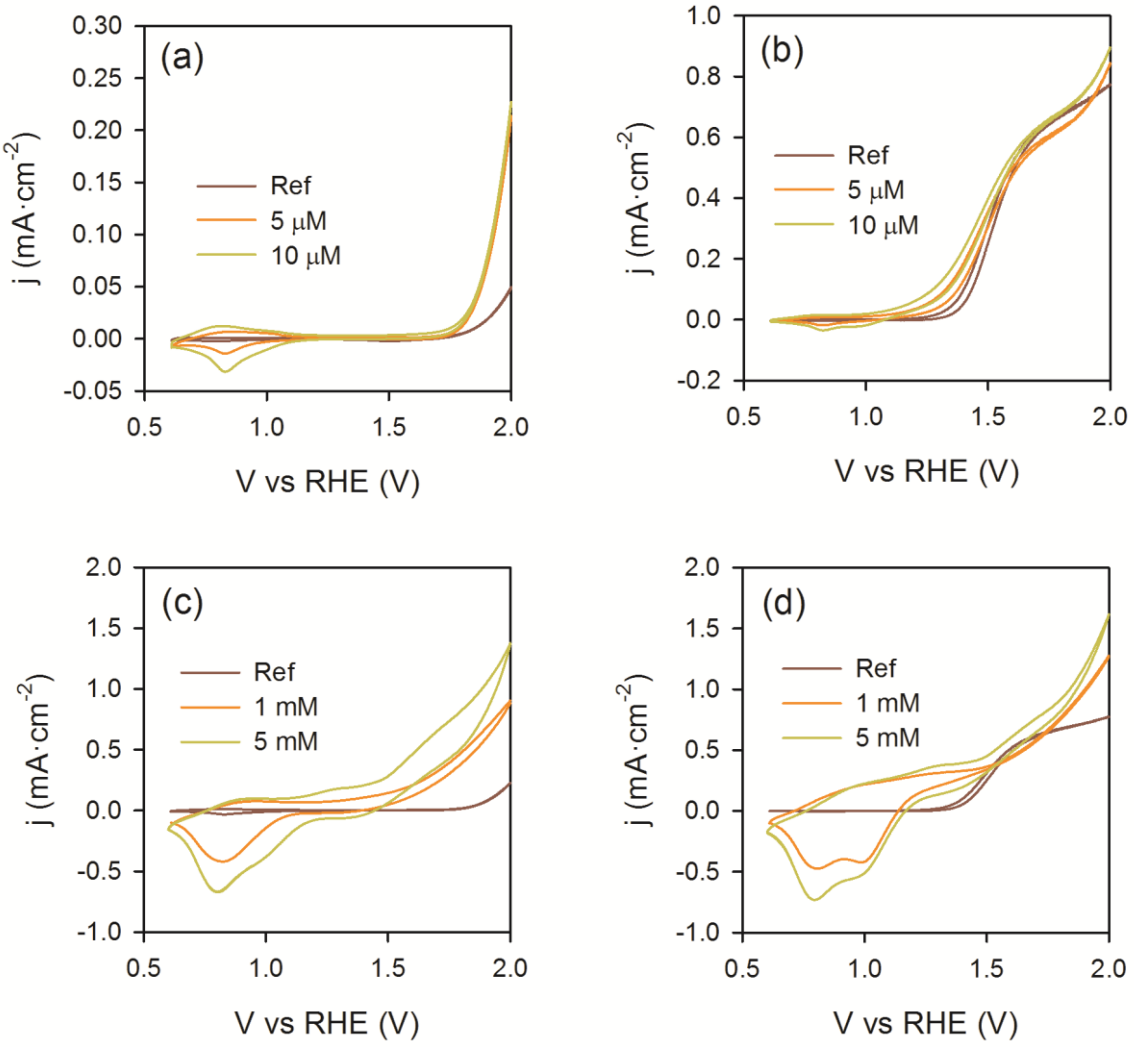
(a)
Ref
5 μM
10 μM
j (mA·cm-2)
V vs RHE (V)
(b)
Ref
5 μM
10 μM
j (mA·cm-2)
V vs RHE (V)
(c)
Ref
1 mM
5 mM
j (mA·cm-2)
V vs RHE (V)
(d)
Ref
1 mM
5 mM
j (mA·cm-2)
V vs RHE (V)

Fig. 3.

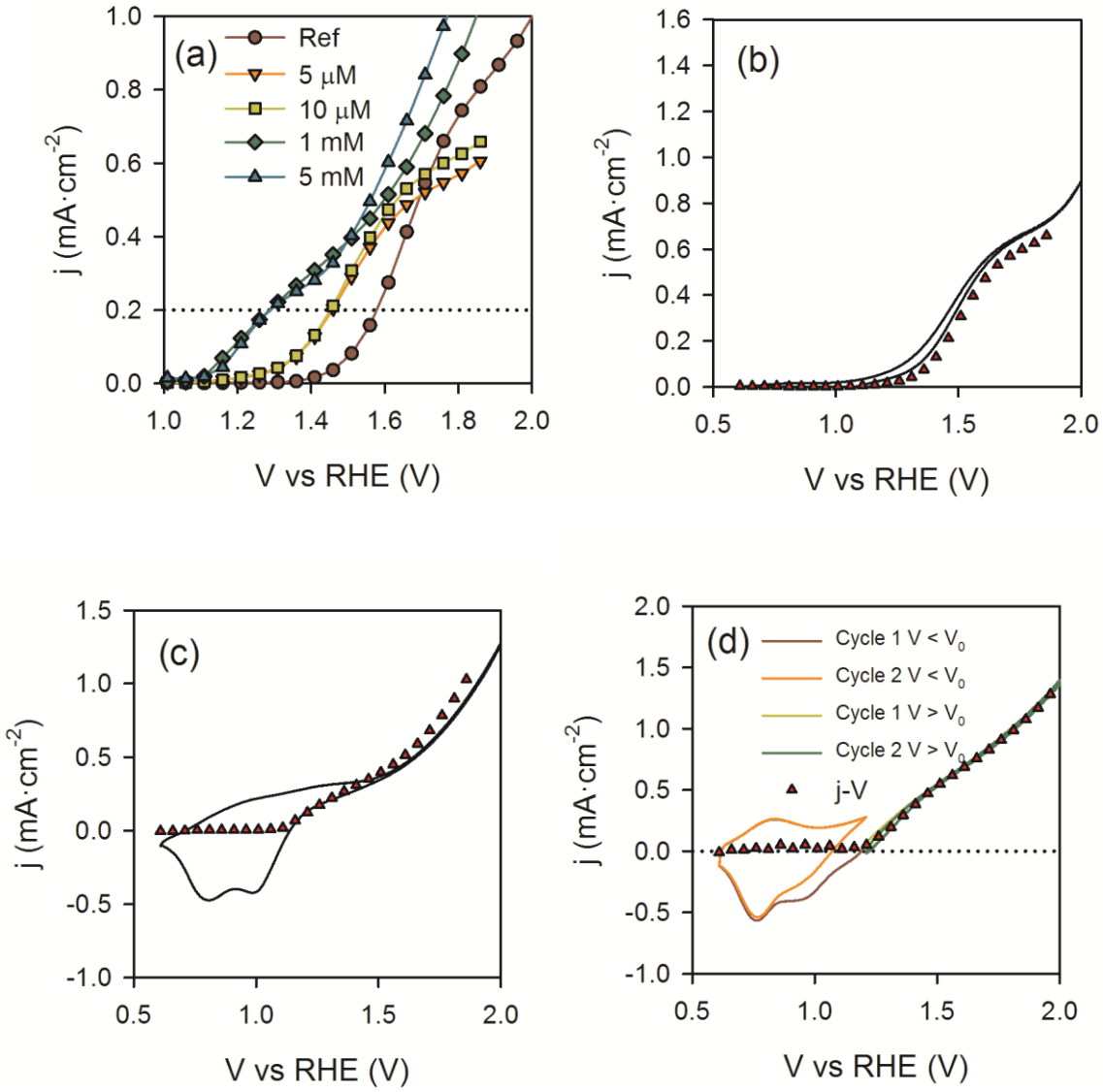
(a)
Ref
5 μM
10 μM
1 mM
5 mM
j (mA·cm-2)
V vs RHE (V)
(b)
j (mA·cm-2)
V vs RHE (V)
(c)
j (mA·cm-2)
V vs RHE (V)
(d)
Cycle 1 V < V0
Cycle 2 V < V0
Cycle 1 V > V0
Cycle 2 V > V0
j-V
j (mA·cm-2)
V vs RHE (V)

Fig. 4.

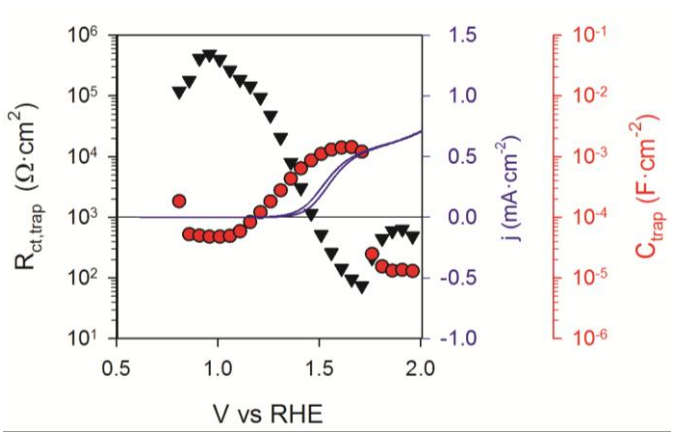
10^6
10^5
10^4
10^3
10^2
10^1
$R_{ct,trap}$ ($\Omega \cdot cm^2$)
1.5
1.0
0.5
0.0
-0.5
-1.0
j ($mA \cdot cm^{-2}$)
10^{-1}
10^{-2}
10^{-3}
10^{-4}
10^{-5}
10^{-6}
C_{trap} ($F \cdot cm^{-2}$)
0.5
1.0
1.5
2.0
V vs RHE

Fig. 5

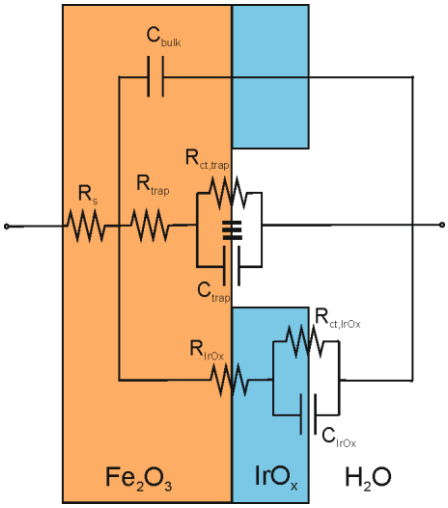
C_bulk
R_ct,trap
R_s
R_trap
C_trap
R_ct,IrOx
R_IrOx
C_IrOx
Fe2O3
IrOx
H2O

Fig. 6.

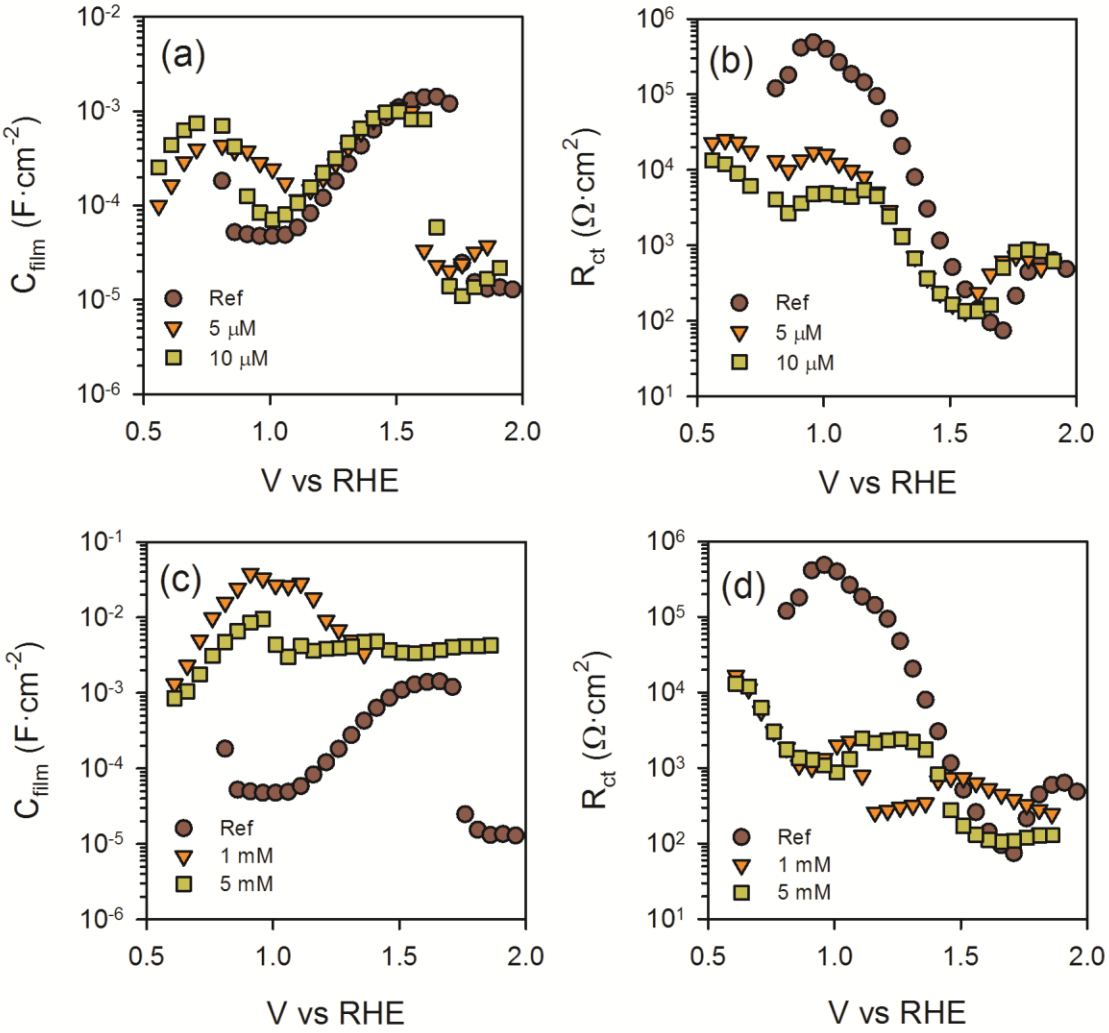

Fig. 7.

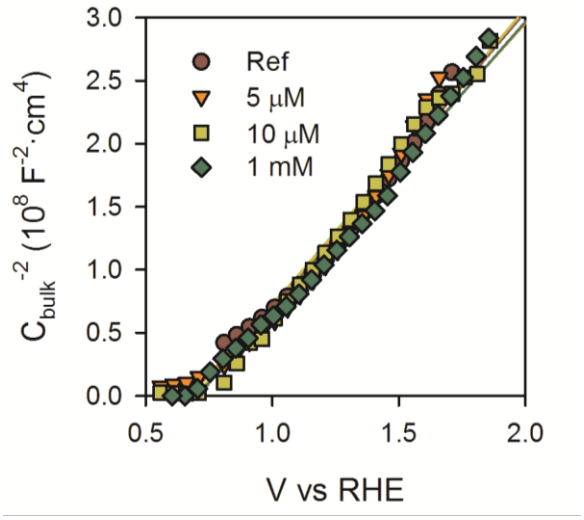
3.0
2.5
2.0
1.5
1.0
0.5
0.0
0.5
1.0
1.5
2.0
Ref
5 μM
10 μM
1 mM
C_{bulk}^{-2} (10^8 $F^{-2}.cm^4$)
V vs RHE

Fig. 8.

Fig. TOC

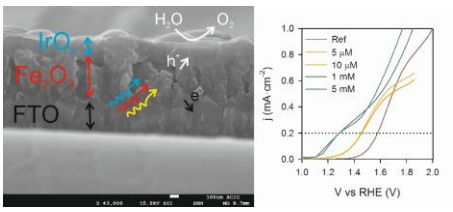

Supplementary Information for the manuscript:

Water oxidation at hematite photoelectrodes with a molecular Iridium catalyst.

Laura Badia-Bou, Elena Mas-Marza, Pau Rodenas, Eva M. Barea, Sixto Gimenez, Eduardo Peris, Juan Bisquert

Photovoltaics and Optoelectronic Devices Group, Departament de Física, Universitat Jaume I, 12071 Castelló, Spain

Dept Quim Inorgan & Organ, Universitat Jaume I, 12071, Castellon de La Plana, Spain

Supporting Information SI1. XPS spectra

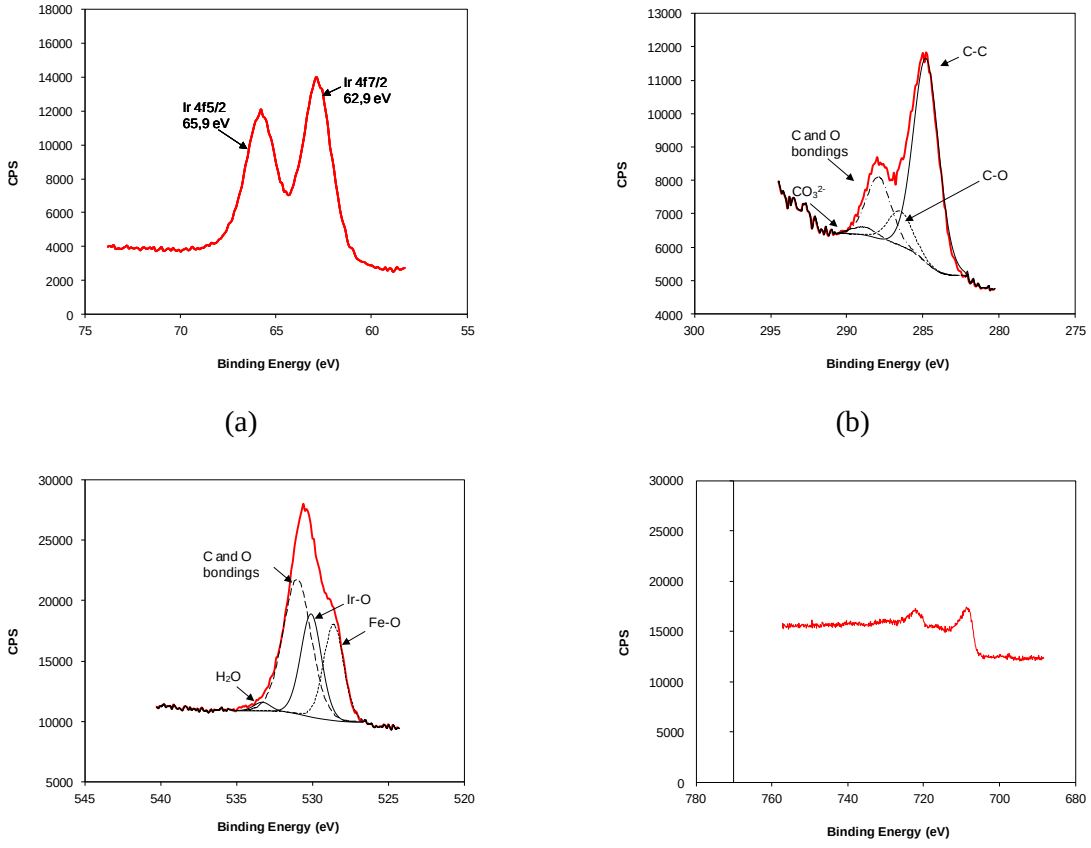

(a) (b)

(c) (d)

Figure SI1.- XPS spectra obtained from a sample Fe_2O_3/IrO_x with Ir deposited from a 5 mM [Cp*Ir] solution (a) Ir (b) C, (c) O , (d) Fe

Supporting Information, SI2. Absorbance spectra of the Fe_2O_3/IrOx samples.

The absorbance spectra were obtained from diffuse reflectance measurements, $A = -\log(R)$ using an integration sphere coupled to the UV-VIR-NIR 5000 Varian Photospectroscometer.

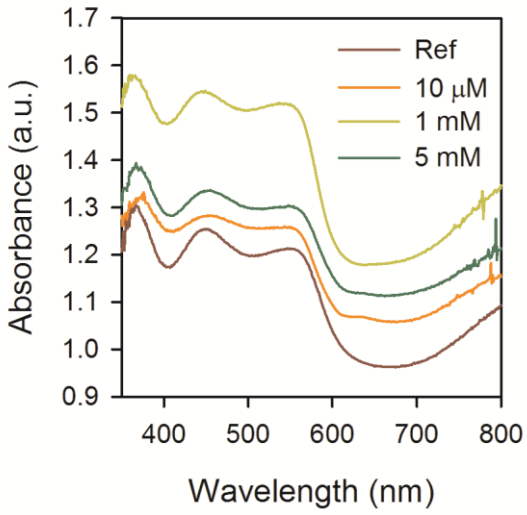

Figure SI2.- Absorbance spectra obtained for the Fe_2O_3/IrOx samples.

Supporting Information, SI3. Cyclic voltammetry curves and steady state j-V from impedance spectroscopy measurements.

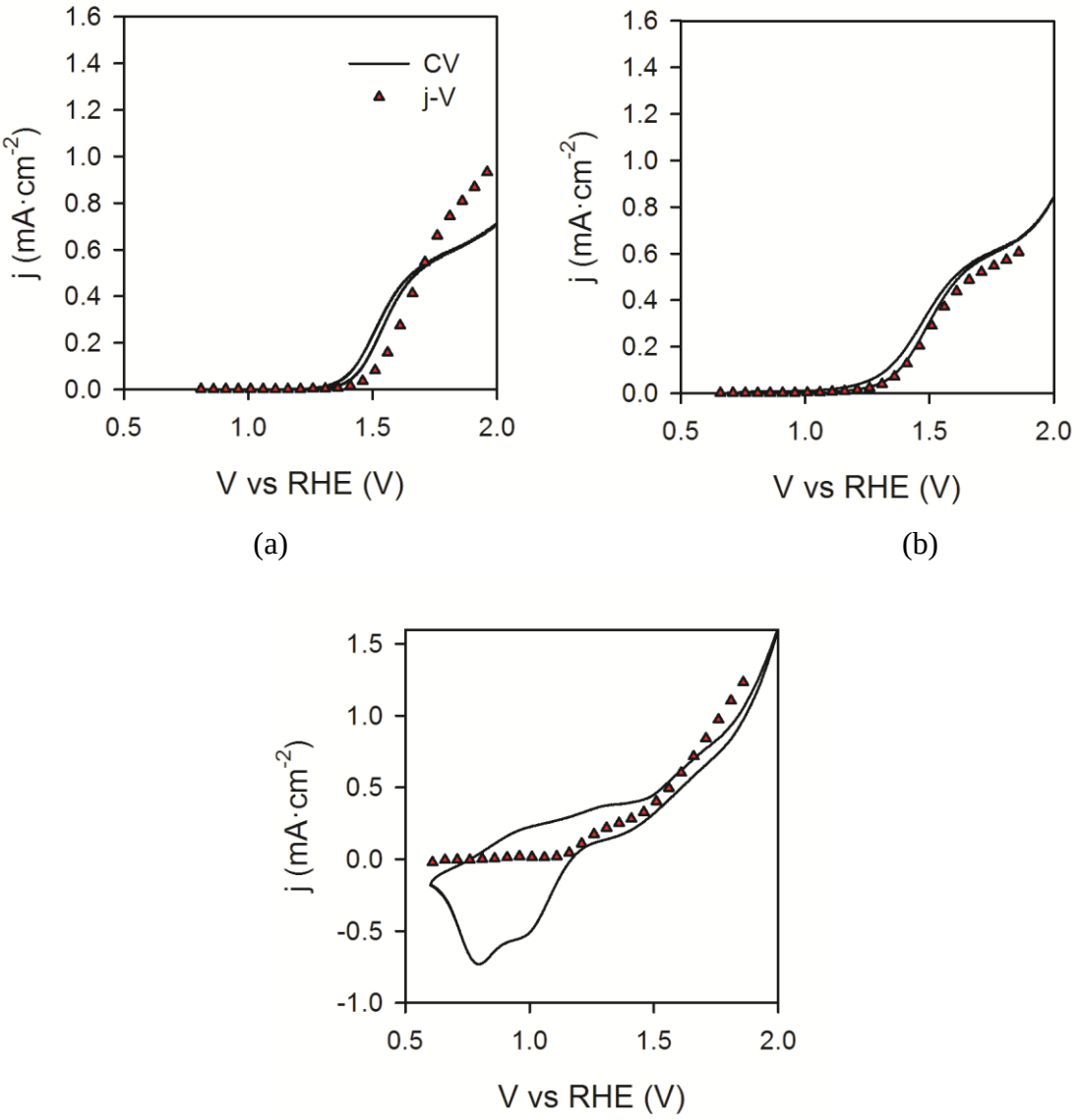

Figure SI3.- Comparison between cyclic voltammetry j-V curves (lines) and steady-state j-V curves (dots) for samples containing different concentrations of the Iridium complex (a) Reference Fe_2O_3 sample, (b) Fe_2O_3/IrO_x sample with Ir source taken from 5 μM [Cp*Ir] solution and (c) Fe_2O_3/IrO_x sample with Ir source taken from 5 mM [Cp*Ir] solution.

Supporting Information, SI4.- Cyclic voltammetry curves of Fe_2O_3/IrO_x (from 10 mM and 1 mM [Cp*Ir] concentrations) in order to rule out IrO_x oxidation contributing to the positive current.

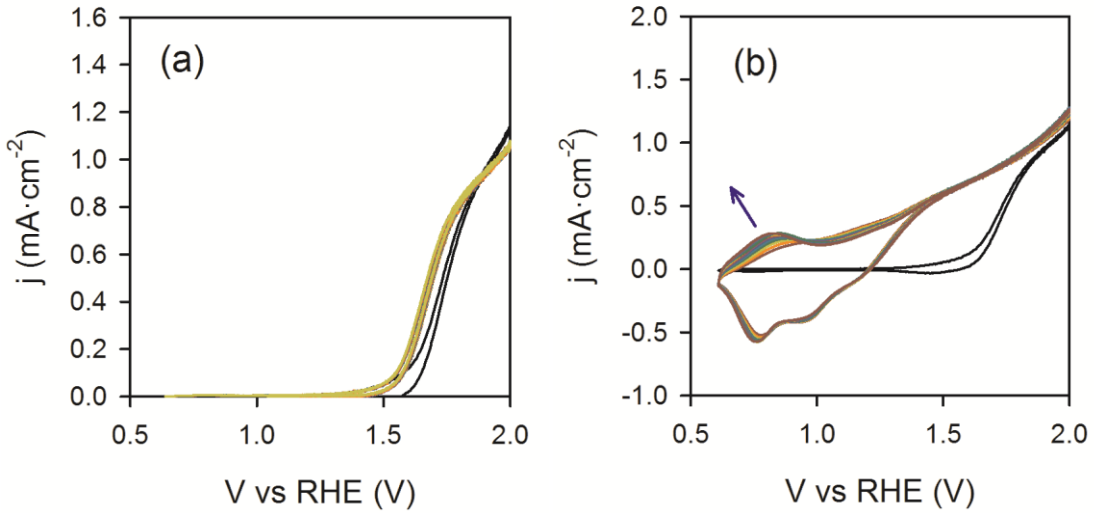

Figure SI4.- 20 consecutive cyclic voltammetry scans for Fe_2O_3/IrO_x samples with Ir source taken from (a) 10 μM [Cp*Ir] solution and (b) 1 mM [Cp*Ir] solution. The arrow indicates de shift of the curves with the number of cycles. The black curves correspond to the reference Fe_2O_3 sample. The highly reproducible repeatability of the scans for (a) indicates that irreversible IrO_x oxidation did not take place during the measurements. Conversely, the shift of the cyclic voltammetry curves with the number of cycles observed in (b) suggests that progressive IrO_x oxidation can take place. However, this effect if clearly separated from the steady-state photocurrent reported in Figure 4.

Supporting Information SI5. Physical model for water splitting with Fe_2O_3 highlighting the role of the surface states and associated equivalent circuits to analyze the experimental impedance spectroscopy data.

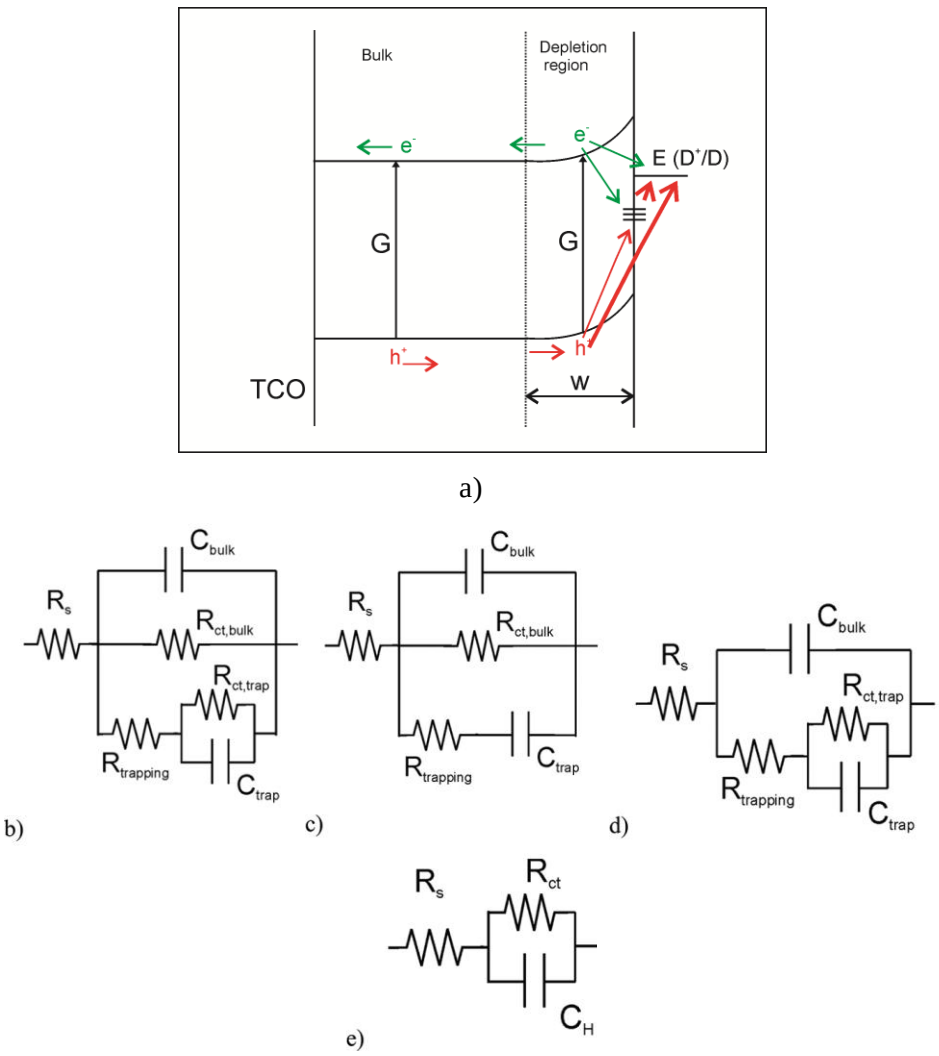

Figure SI5. Physical model for the charge carriers dynamics in hematite electrodes, showing their generation, G, by light absorption, surface state trapping, and interfacial charge-transfer reactions. (b) Equivalent circuit corresponding to physical model in part a. (c) Simplified model used for IS interpretation created by removing $R_{ct,trap}$. (c) . (d) Simplified model used for IS interpretation created by removing $R_{ct,bulk}$ (e) Randles circuit.

Supporting Information SI6.- Examples of impedance spectra obtained for Fe_2O_3 and Fe_2O_3/IrOx samples and fitting to the physical model.

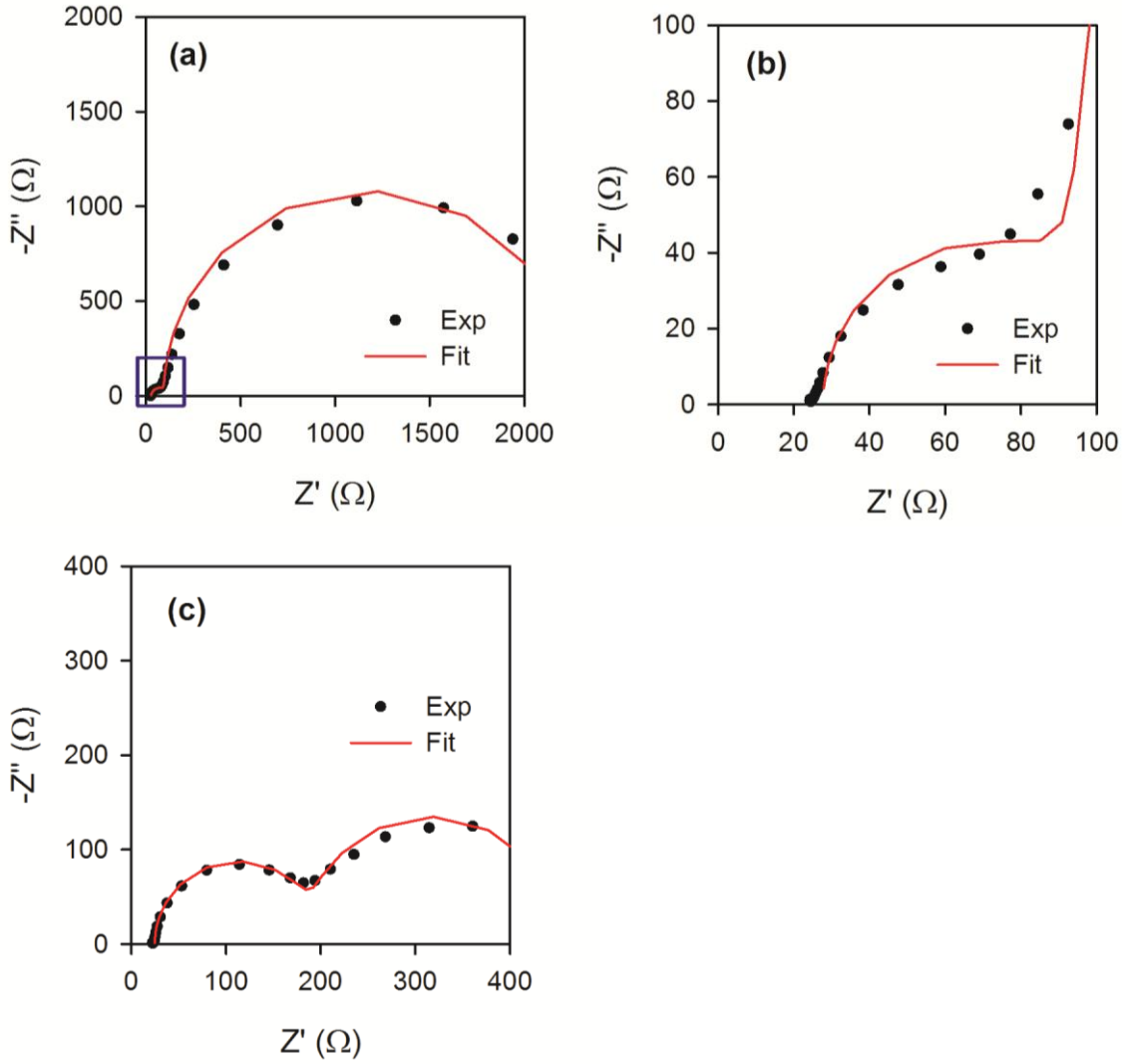

Figure SI6.- (a) Nyquist plot and fitting curve to the model detailed in Figure SI5 of bare Fe_2O_3 at V=1.41 V vs RHE (b) Magnification of the high frequency region framed by a blue square in (a). (c) Nyquist plot and fitting curve to the model detailed in Figure 6 of Fe_2O_3/IrO_x (5 mM solution) at V=1.46 V vs RHE. The fitting error was systematically below 5% for all the spectra and all the extracted parameters.

Supporting Information, SI7. Relationship between photocurrent (j), charge transfer resistance (R_{ct}) and capacitance (C_{film}).

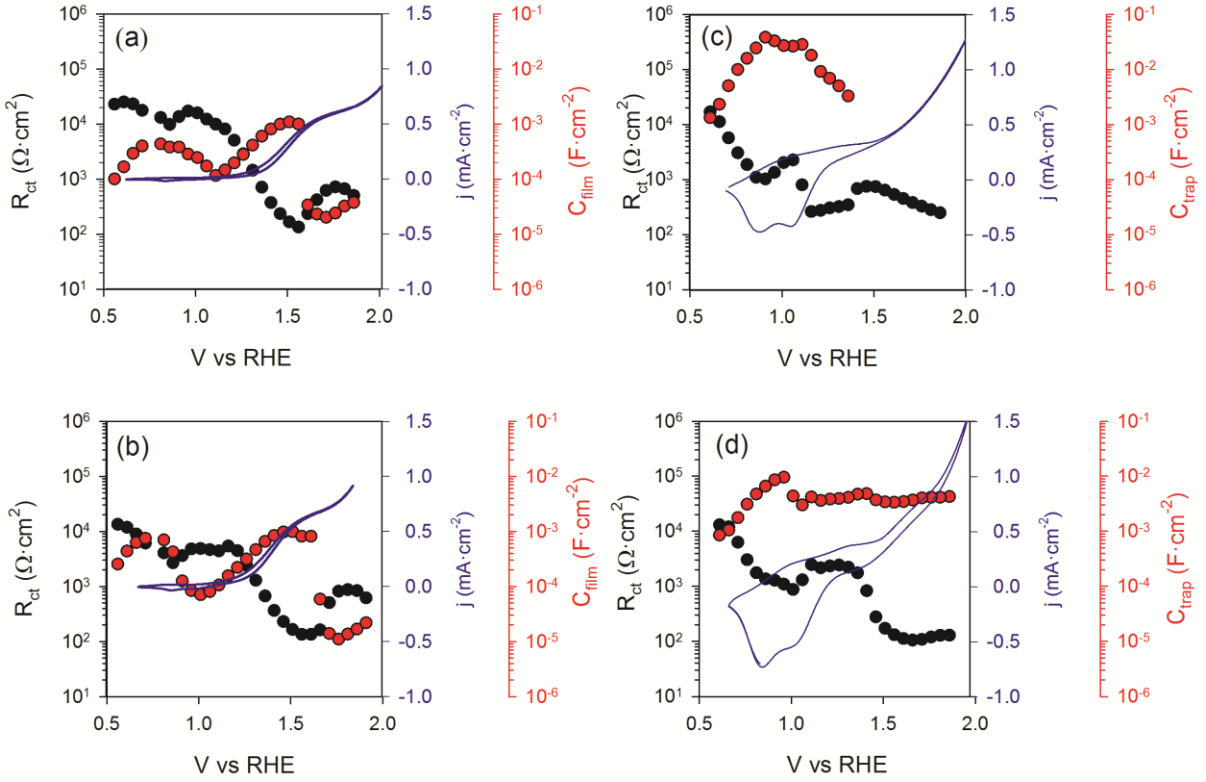

Figure SI7.- Photocurrent (j), charge transfer resistance (R_{ct}) and capacitance (C_{film}) for Fe_2O_3 films with IrO_x films deposited from solutions with different concentrations of [Cp*Ir] (a) 5 µM, (b) 10 µM, (c) 1 mM and (d) 5 mM.